CHALMERS
UNIVERSITY OF TECHNOLOGY

Effect of heat exchanger integration in aerodynamic optimization of an aggressive S-duct

33RD CONGRESS
OF THE INTERNATIONAL COUNCIL
OF THE AERONAUTICAL SCIENCES
STOCKHOLM, SWEDEN, 4-9 SEPTEMBER, 2022

ICAS 2022 SWEDEN

EFFECT OF HEAT EXCHANGER INTEGRATION IN AERODYNAMIC OPTIMISATION OF AN AGGRESSIVE S-DUCT

Isak Jonsson[1], Robert Ranman[1], Alexandre Capitao[1] & Carlos Xisto[1]

[1]Chalmers University of Technology, Gothenburg, SE-41296, Sweden

Abstract

Intercooling the core flow in the compression process using bypass air can potentially reduce fuel consumption in commercial aviation. However, one of the critical challenges with intercooling is the installation and weight penalty due to complex ducting and large surface area for air-to-air heat exchangers (HEX). The recent interest in cryogenic hydrogen (LH2) as a potentially carbon-neutral fuel for commercial aviation expands the propulsive system's design space due to the vastly different fuel properties between classical Jet-A and LH2. Regarding intercooling, LH2 adds a formidable heat sink with a high specific heat capacity and low storage temperature at 20K and, if utilised in the intercooling process, should allow for increased cooling power density with less installation penalties than an air-to-air HEX. Furthermore, the heat is transferred to the fuel instead of ejected into the bypass air which has potential thermodynamical benefits. The HEX can further be synergistically used to radial turn the core flow in the ICD.

This paper presents the integration of a compact air-to-LH2 heat exchanger inside the gas path of the intermediate compressor duct (ICD) as the shape of a truncated cone. Axisymmetric numerical simulations are utilised to evaluate the duct performance and optimise hub and shroud lines for minimal pressure drop and outlet uniformity. The HEX sizing was based on a preliminary system model of an LH2 commercial aviation engine with 70,000 lbs of thrust.

Keywords: Low-pressure compressor, intermediate compressor duct, numerical simulations, cryogenic hydrogen.

1. Introduction

Intercooled gas turbines are commonly found in stationary and marine applications due to the intercooling benefits to the gas turbine cycle [11, 4, 19, 14]. However, even though seriously considered in several studies and configurations [2, 16, 9, 17, 12] there are no flying intercooled commercial jet engines today. Arguably, the lack of intercoolers in the aviation industry can largely be explained by the considerably higher performance penalties in aviation due to increased weight and size relative to marine or stationary gas-turbine installations.

Hydrogen fuelled aircraft might address some of the issues with intercooling in aviation. Hydrogen, relative to other potential carbon-neutral aviation fuels, has a high gravimetric energy density but a low volumetric energy density. A large part of the volumetric disadvantage can be mitigated by storing hydrogen at cryogenic temperatures. Cryogenic hydrogen (LH2) as a coolant provides a high temperature difference to the core flow, allowing for high power density heat exchanger (HEX). In addition, the high specific heat capacity of LH2 allows for relatively small cooling channels, which further increases the power density of the HEX. Finally, the heat from the core flow is not rejected into the bypass air but into the fuel, which is thermodynamically beneficial from a system perspective.

The current work focuses on installing the HEX inside the intermediate compressor duct (ICD) between the high-pressure compressor (HPC) and low-pressure compressor (LPC). The ICD allows for traditional high-density HEX without substantial modification to the LPC and HPC. The ICD is an annular duct that radially guides the flow from the larger radius of the low-pressure compressor to the lower radius of the high-pressure compressor. These s-ducts are typically designed for maximum

turning with acceptable pressure losses. The design of an ICD is determined by the development of boundary layer at the end-walls. As the duct length is reduced, the turning increases and the adverse pressure gradient eventually causes one of the two boundary layers to separate. Several approaches have been presented to suppress a separation and allow for more aggressive ICDs. For example, Walker et. al. [15] used compressor bleed to remove the low momentum boundary layer away at the hub, Taylor et. al. [13] successfully integrated splitters allowing for a super aggressive s-duct design, and Jonsson [8] showed early design attempts in heat exchanger integration in the ICD by splitter vanes.

For an ICD with an integrated HEX, the pumping losses relative to heating power has to be considered. The relation between heat-transfer $\dot{Q}$ to pumping power $\dot{W}$ for an ideal heat exchanger, assuming fully developed boundary layers, can be estimated by Eq. (1), derived in [18]. From Eq. (1) on may note that the ratio of heat to pumping losses decreases with the square of Mach number M, and hence flow diffusion, leading to an increased heat-exchanger face area and short length, is beneficial to reduce the pumping work for a targeted heating power. The normalised temperature difference θ scales linearly to the heating power, and C_p is the fluid specific heat capacity.

$$\frac{\dot{Q}}{\dot{W}} = \frac{C_p \theta a^2}{M^2} \tag{1}$$

Diffusion with attached boundary layers causes an adverse pressure gradient. As mentioned before, the ICD is primarily limited by an boundary separation caused by a strong adverse pressure gradient, so with all else equal, increasing diffusion will have a negative impact on the turning ability of the ICD. Diffuser performance is typically displayed as the pressure rise coefficient defined in Eq. (2), which scales the static pressure rise to the inlet dynamic pressure, where p_{st} is the stagnation pressure and p_0 is the total pressure for the inlet in and outlet out.

$$C_{pr} = \frac{p_{st,out} - p_{st,in}}{p_{0,in} - p_{st,in}} \tag{2}$$

1.1 Approach

Preliminary studies, similar to the ones reported in [1] were performed using Chalmers in-house gas turbine performance tool GESTPAN [5] to size the intercooler located between the LPC and HPC. The preliminary results indicated a diffusion factor of 4.4 between the outlet of the LPC and the inlet of HEX to be suitable. With traditional annular diffusers, a non-stalling diffuser would be longer than the entire conventional ICD, as defined in [7]. Adding turning and acceleration demands to the ICD seemed unlikely to function satisfactorily. Instead, the HEX was manually fitted to gradually bleed through the core flow and aid the turning of the flow radially by selecting fin-tube HEX. An initial design was evaluated by manual adjustment and numerical simulations and later used as a starting point for aerodynamic optimisation.

An isometric view of the initial design is illustrated in Fig. 1 with a fin-tube type HEX shaped truncated cone spanning the ICD gas path. The HEX is placed at the OGV outlet near the hub with an increasing radius in the axial direction. The core flow gradually passes through the HEX and achieves the required area ratio. The HEX fins guide the flow radially and aid in the radial turning of the ICD. After the HEX, the cross-section is reduced to match the outlet.

The ICD with the integrated HEX is compared against a traditional ICD s-duct which has been optimised using identical optimisation target functions, simulation methods and inlet and outlet conditions and geometrical constraints.

1.2 Numerical Setup

The axisymmetrical simulations are performed with the commercial software Fluent^{TM} R19.1 with steady-state Reynolds-Averaged Navier-Stokes simulations (RANS) using the $k-\omega$ SST model with a near-wall mesh refinement and density-based solver applicable for compressible flows [6]. Simulations were performed using a total pressure boundary at the inlet and adjusting the outlet static pressure to achieve the target mass flow. The total pressure loss over the HEX is modelled utilising

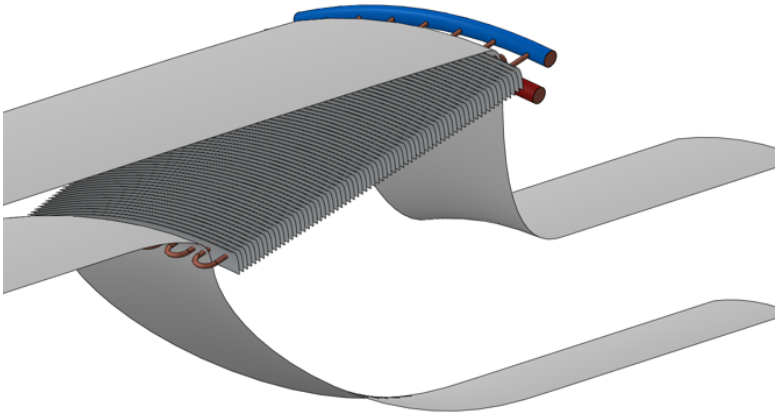

Figure 1 – Isometric view of a initial integration of fin-tube heat exchanger into an ICD. The core flow enters left and exists to the right while the blue and red tube represent coolant inlet and outlet respectively

the power-law model [6] shown in Eq. 3. The coefficients C_0 and C_1 are derived from empirical data of industrial HEX.

$$S_i = -C_0|v|^{C_1} \tag{3}$$

The internal fins in the HEX are modelled by implementing a directional resistance dependency in the porous media. The viscous resistance along the normal of the HEX surface follows the before mentioned empirical correlation while any orthogonal resistance is set to several orders of magnitude higher, effectively replicating the fins by restricting the flow in the normal direction.

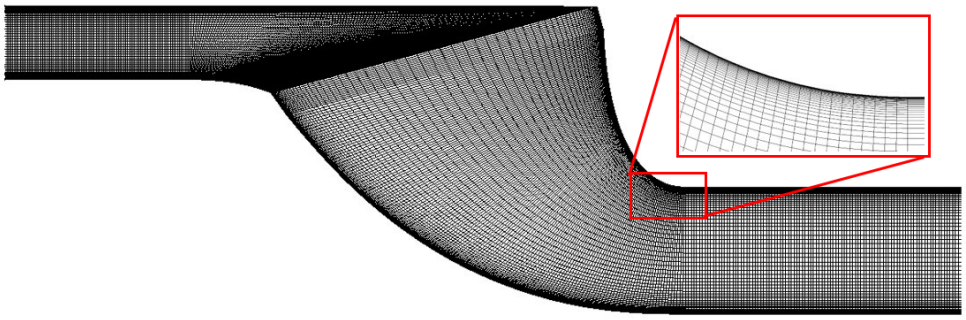

Figure 2 – Example mesh from the optimisation population

A hexahedral mesh is generated in ICEMCFD^{TM} and shown in Fig. 2. A mesh study of the conventional duct was used to down-select a suitable refinement in terms of valid results and computational cost. The baseline case was initialised with a mesh cell count of 300,000 elements throughout the domain, working up to approximately 900,000 elements. Mesh convergence criteria was selected as when relative change Y_p was below 1% which was found at a domain mesh refinement of approximately 700,000. All meshes were refined to provide a $y^+ < 1$.

The algorithm used for optimization is a simple genetic algorithm (SGA) provided by the open-source framework openmdao [3]. Initial sampling size, $N_{samples}$, is obtained as a function of the dimension, D, of the problem i.e. number of design variables, sufficiently covering the parametric space constrained to a maximum of 100 generations.

$$N_{samples} = \frac{(D+1)(D+2)}{2} \tag{4}$$

Parameterisation & Objective

The four Bézier curves that define the domain for the diffuser upstream the HEX and the contraction downstream the HEX are shown in Fig. 3a-b as blue lines. A sequence of points p_n, shown as red points in Fig. 3a-b controls each Bézier curve and are optimised utilising a multi-objective approach coupled with a genetic algorithm. Geometrical constraints are enforced by locking or limiting relations between the control points. For example, the inlet and outlet are parallel to the rotational axis by locking selected control points radially. In addition, the negative volumes at the interface between the shroud and HEX are mitigated by geometrical constraints on the nearest control points. The aero surfaces for the traditional ICD are defined with two bézier curves and shown as blue lines in Fig. 3b. One may note that the number of control points, marked with red points, are fewer in the traditional case Fig. 3b compared to the HEX integrated ICD Fig. 3a. The inlet and outlet constraints are, however, identical.

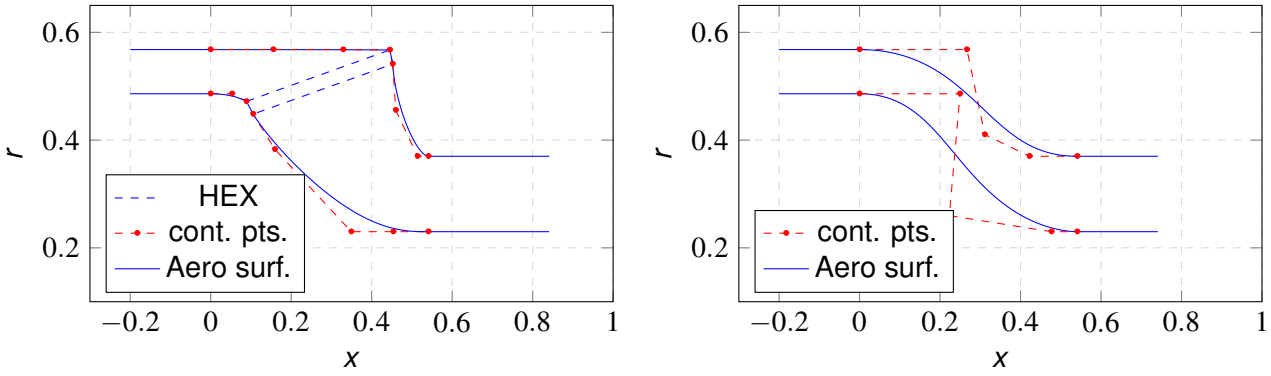

Figure 3 – Section view of the initial HEX integration in the ICD with aerosurface, hex position and thickness and control points to the left. A section view of the traditional duct is shown in the same matter to the right. Core flow enters from the left.

The first objective function is total pressure loss across the duct relative to inlet stagnation pressure (Y_p), as defined in Eq. (5), where P_0 is mass-flow average total pressures at the inlet in and outlet out. If not otherwise specified, the location i in Eq. (5) is at the outlet of the domain. However, for particular studies inside the ICD, the position i is an intermediate position. The second objective function is the flow non-uniformity (σ) which is defined in Eq. (6) of the outlet flow.

$$Y_p = \frac{P_{0,i} - P_{0,out}}{P_{0,in}} \tag{5}$$

The level of uniformity in the outflow stream is measured at half the outlet length computed from the velocity magnitude and evenly distributed points.

$$\sigma = \sqrt{\frac{\sum_{i=1}^{n} A_i (x_i - \bar{x})^2}{\sum_{i=1}^{n} A_i \bar{x}^2}}, \qquad x = V, p_0 \tag{6}$$

Y_p is the primary objective of the optimisation loop and is therefore weighted against the outflow uniformity with a weight of 0.2.

2. Results

Figure 4a-b shows the population of the two optimisations as black markers in regards to the design objective of non-uniformity σ along the vertical axis and total pressure losses Y_p along the horizontal axis. One case from each population is selected for further studies, which is marked out with a red marker. The traditional ICD in Fig. 4b converges at a loss coefficient of around 0.019, which is similar to the lower end of what is presented for a conventional duct in [10]. From Fig. 4b, one may note that an increased non-uniformity is in general correlated with an increased loss coefficient which indicates that the two objectives are not very octagonal. From an ideal case, this is expected as a

fully attached flow with a thin boundary layer would generally produce low losses and non-uniformity coefficient. There is an outlier marked with a blue marker in Fig 4b is neglected due to non-physical results. Regarding the ICD with the integrated HEX, the selected case was the one with the lowest pressure losses of an Y_p of 0.0744. One may note that the range of non-uniformity σ is reduced in Fig 4a compared to b. The aforementioned is logical since the HEX counteracts flow non-uniformity and a rapid contraction facilitates more control over flow distribution than a traditional open ICD.

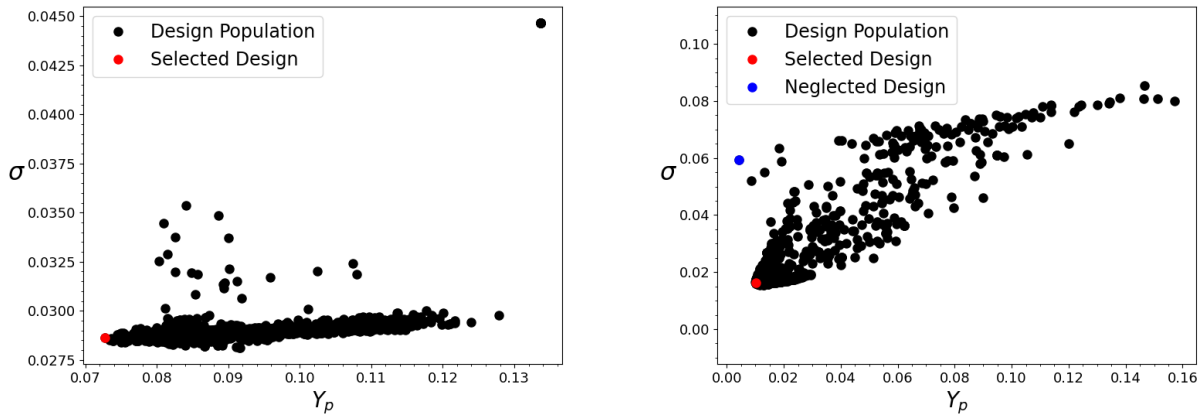

Figure 4 – Optimisation population in regard to the objective, non-uniformity σ and pressure loss Y_p for the HEX integrated duct (left) and the traditional ICD duct (right). The selected cases are marked with a red marker for both the ICD and heat exchanger integrated duct (HID). Blue circle marks a case which was disregarded for further studies.

In Figure 5 the geometry of the two selected designs from the optimisation populations is overlayed in the same domain. The ICD is shown as solid black lines, while the hub and shroud lines of the HID are shown as solid blue lines with the HEX domain as shaded blue. The location of boundaries of interest is marked out in the same figure as dashed red lines, with the identifier later used when presenting and discussing integrated boundary values and radial distributions. Note that the boundary for HEX inlet $._{H_{in}}$ and outlet $._{H_{outlet}}$ are placed slightly outside the porous domain and not on the boundary itself to capture free stream to avoid interference from the HEX modelling.

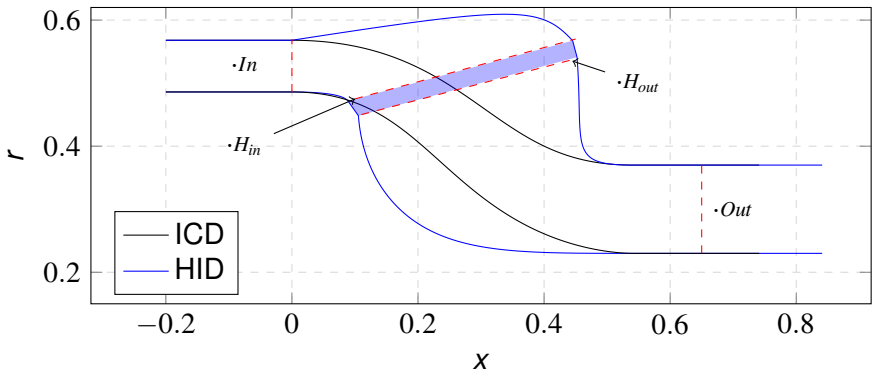

Figure 5 – The two selected designs are shown with the solid blue lines for the HID and the black lines for the ICD together with the investigation boundaries marked out with dashed red lines.

Figure 6 shows the mass flow average losses in terms of Y_p between the selected boundaries along the vertical axis and the selected boundary differential along the horizontal axis. The column named Total is the difference between the inlet and outlet boundary layer, the column Diffuser is differential between the boundary $._{In}$ and $._{H_{in}}$, HEX between $._{H_{in}}$ and $._{H_{out}}$, and Contraction between $._{H_{Out}}$ and $._{Out}$. From Fig. 6a, one may note that the majority of the losses in the selected HEX ICD is over the

heat exchanger. The losses in the diffuser and contraction are approximately 50% larger to the total losses in the ICD where the majority of the losses occur in the diffuser.

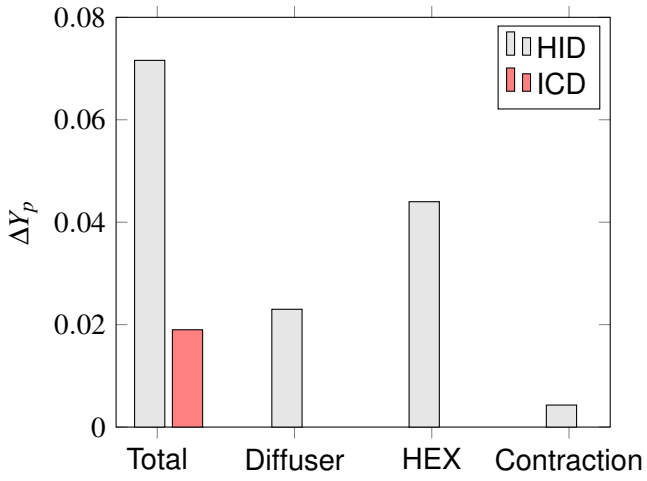

Figure 6 – The loss distribution in the diffuser, HEX and contraction for the selected configuration.
To the right is

Figure 7a and b show the radial distribution of normalised velocity magnitude and loss coefficient for both the HID and the ICD. The velocity distribution at the outlet marked as a solid blue line for the HID and dashed black lines for the ICD show that the outlet distribution from the HID is substantially flatter compared to the outlet of the ICD. The outlet velocity from the HID is also approximately 10% higher compared to the ICD due to the reduced air density caused by the rise in static temperature due to viscous losses and pressure drop over the HEX. Further upstream, at the inlet and outlet of the HEX, illustrated with red and black solid lines, near static flow is seen for the first 1-5% near the hub. The velocity distribution into and out of the HEX is otherwise generally leaned towards the shroud, where a boundary layer buildup can be observed for the last 5-7% of the span. In Figure 7b the outlet between the ICD and the HID is shifted by and an average of 0.074, but similar trends as for the velocity outlet can be observed where the HID outlet is significantly more uniform compared to the ICD. At the inlet of the HEX, the Y_p distribution leans towards the shroud with areas of higher Y_p above 80% span compared to inlet Y_p and high losses below 20% span. The majority of the Y_p non-uniformity is reduced through the HEX, as observed at Y_p distribution at the outlet of the HEX . There is, however, very little flow through the HEX below 5% of span.
The Mach numbers inside ICD with integrated HEX are shown in Fig. 8. The average Mach number at the inlet is 0.45 and is reduced as the flow decelerates through the diffuser. As described in the paragraph above, one can notice the boundary buildup near the shroud and hub in the diffuser. Even though it is not possible to deduce from the figure Fig. 8, the author would like to comment that there is only reversed flow near the hub. In the contraction, the flow is accelerated to create a uniform outlet from the relatively uneven HEX outlet. One can note a high acceleration zone a the shroud just before the outlet as the flow is turned axially with Mach numbers approaching one.

3. Conclusion

This paper shows the successful integration of a pre-defined and positioned compact air-to-LH2 HEX fitted inside the ICD with limited geometrical and aerodynamic installation penalties. The current concept includes an ultra-short diffusing sector with a high recovery factor, a HEX module and contraction. From a system modelling perspective, the aerodynamic installation penalties can be integrated by applying a 50% increase in duct losses compared to an optimised traditional ICD. Furthermore, the geometrical installation penalties are relatively limited, with only a minor expansion of the hub and shroud lines in the ICD required.
The presented results are case-specific and include several limitations and simplifications that could arguably be non-engine representative. For example, modern engines rarely see a pure axial inlet

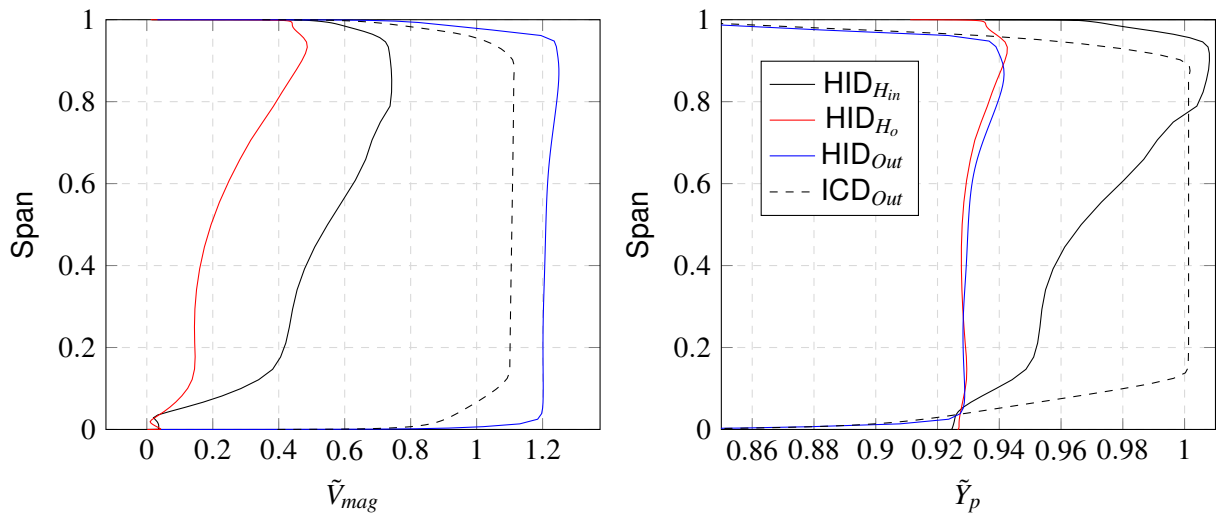

(a) (b)

Figure 7 – Radial distributions of a) normalised velocity magnitude and b) normalised total pressure loss coefficient $\tilde{Y}_p$. The results are computed at the inlet of the HEX, outlet of the HEX and the outlet of the ICD along the normalised span.

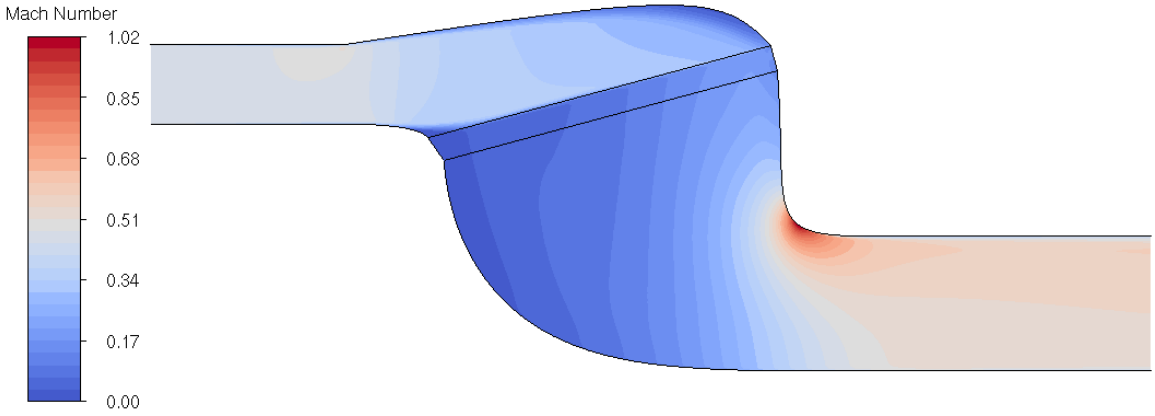

Figure 8 – Contours of Mach number in the selected ICD with integrated HEX.

and outlet ducts and the relatively high LPC outlet Mach number of 0.45. However, these were selected to emphasise the challenges of the diffuser design. There are also several simplifications in the modelling aspects by using axisymmetric RANS simulation, locked HEX sizing and position and no heat transfer, which is likely to produce a non-optimal solution set. However, the current study provides several insights into the feasibility of the presented HEX implementation concept.

In LH2 intercooling concepts, there is a significant potential to utilise an inclined HEX since it allows for an ultra-short diffuser in relation to traditional diffusers. The current study with the aforementioned limitation managed to diffuse the flow for most of the HEX, and the pressure losses over the HEX were only parts of a percent higher compared to an ideal case when the flow is uniformly distributed over the HEX. An optimisation that allows for the HEX's movement would likely produce lower losses in the diffusion section and a more uniform flow over the HEX, thereby creating a better solution overall.

A secondary benefit is the increased control of the ICD outlet velocity profile that the HEX and contraction provide. For the current optimisation, this increased control provided thinner end wall boundary layers compared to a traditional duct, which could prove beneficial in the design of the HPC.

4. Acknowledgement

The E.U. financially supports this work under the “ENABLEH2 – Enabling cryogenic hydrogen-based CO2 free air transport” Project co-funded by the European Commission within the Horizon 2020 Programme (2014-2020) under Grant Agreement no. 769241. The authors also acknowledge the support provided by the department of Mechanics and Maritime Sciences at Chalmers University of Technology.

5. Copyright Statement

References

[1] H. Abedi, C. Xisto, I. Jonsson, T. Grönstedt, and A. Rolt. Preliminary analysis of compression system integrated heat management concepts using lh2-based parametric gas turbine model. *Aerospace*, 9(4), 2022.

[2] C. A'Barrow, J. F. Carrotte, A. D. Walker, and A. Rolt. Aerodynamic performance of a coolant flow off-take downstream of an ogv. In *Turbo Expo: Power for Land, Sea, and Air*, volume 54679, pages 187–199, 2011.

[3] J. S. Gray, J. T. Hwang, J. R. R. A. Martins, K. T. Moore, and B. A. Naylor. OpenMDAO: An open-source framework for multidisciplinary design, analysis, and optimization. *Structural and Multidisciplinary Optimization*, 59(4):1075–1104, April 2019.

[4] H. Grieb. *Projektierung von Turboflugtriebwerken*. The MIT Press, 09 2004.

[5] T. Grönstedt. *Development of methods for analysis and optimization of complex jet engine systems*. Chalmers Tekniska Hogskola (Sweden), 2000.

[6] A. Inc. *Fluent Theory Guide - 2021-R1*. Ansys Inc, 2021.

[7] I. Jonsson. *Experimental Aerothermal Study of Internal Jet Engine Structures*. Chalmers Tekniska Hogskola (Sweden), 2022.

[8] I. Jonsson, C. Xisto, H. Abedi, T. Grönstedt, and M. Lejon. Feasibility Study of a Radical Vane-Integrated Heat Exchanger for Turbofan Engine Applications. volume Volume 7C: Heat Transfer of *Turbo Expo: Power for Land, Sea, and Air*, 09 2020. V07CT13A019.

[9] P.-W. Kwan, D. R. Gillespie, R. D. Stieger, and A. M. Rolt. Minimising loss in a heat exchanger installation for an intercooled turbofan engine. In *Turbo Expo: Power for Land, Sea, and Air*, volume 54617, pages 189–200, 2011.

[10] C. Ortiz Duenas, R. J. Miller, H. P. Hodson, and J. P. Longley. Effect of Length on Compressor Inter-Stage Duct Performance. volume Volume 6: Turbo Expo 2007, Parts A and B of *Turbo Expo: Power for Land, Sea, and Air*, pages 319–329, 05 2007.

[11] P. Papadopoulos and P. Pilidis. Introduction of intercooling in a high bypass jet engine. In *ASME 2000-GT-150*, 2000.

[12] A. Rolt and N. Baker. Intercooled turbofan engine design and technology research in the eu framework 6 newac programme. *ISABE 2009 Proceedings, Paper No. ISABE-2009-1278*, 2009.

[13] J. V. Taylor, F. Flanagan, A. Dunlop, S. D. Grimshaw, and R. J. Miller. Super Aggressive S-Ducts for Air Breathing Rocket Engines. *Journal of Turbomachinery*, 143(6), 04 2021. 061015.

[14] O. Thulin, O. Petit, C. Xisto, X. Zhao, and T. Grönstedt. First and second law analysis of radical intercooling concepts. *Journal of Engineering for Gas Turbines and Power*, 140(8), 2018.

[15] A. D. Walker, A. G. Barker, and J. F. Carrotte. Numerical Design and Experimental Evaluation of an Aggressive S-Shaped Compressor Transition Duct With Bleed. volume Volume 7: Turbomachinery, Parts A, B, and C of *Turbo Expo: Power for Land, Sea, and Air*, pages 151–161, 06 2011.

[16] A. D. Walker, J. F. Carrotte, and A. M. Rolt. Duct aerodynamics for intercooled aero gas turbines: constraints, concepts and design methodology. In *Turbo Expo: Power for Land, Sea, and Air*, volume 48883, pages 749–758, 2009.

[17] G. Wilfert, J. Sieber, A. Rolt, N. Baker, A. Touyeras, and S. Colantuoni. New environmental friendly aero engine core concepts. *ISABE Paper*, (2007-1120), 2007.

[18] D. G. Wilson and T. Korakianitis. *The Design of High-Efficiency Turbomachinery and Gas Turbines*. The MIT Press, 09 2014.

[19] X. Zhao. *On Aero Engine Intercooling*. Chalmers Tekniska Hogskola (Sweden), 2013.